

Article

Proposal of Fatigue Limit Design Curves for Additively Manufactured Ti-6Al-4V in a VHCF Regime Using Specimens with Artificial Defects

Yoshihiko Uematsu ^{1,*} , Toshifumi Kakiuchi ¹, Yaodong Han ² and Masaki Nakajima ³

¹ Department of Mechanical Engineering, Gifu University, 1-1 Yanagido, Gifu 501-1193, Japan; kakiuchi@gifu-u.ac.jp

² Graduate School of Natural Science and Technology, Gifu University, 1-1 Yanagido, Gifu 501-1193, Japan; k1o5ah1r@yk.commufa.jp

³ National Institute of Technology, Toyota College, 2-1 Eisei-cho, Toyota, Aichi 471-8525, Japan; yo-nakag@tg.commufa.jp

* Correspondence: yuematsu@gifu-u.ac.jp

Abstract: Cantilever-type rotating bending fatigue tests were conducted under a very high cycle fatigue regime using conventionally manufactured Ti-6Al-4V specimens having drilled artificial defects with different sizes. The relationship between fatigue limit and defect size was defined as a fatigue limit design curve considering the transition from the fracture-mechanics dominating area to the fatigue-limit dominating area. A conventional Murakami's equation was applicable as a design curve of additively manufactured Ti-6Al-4V with defects at 10^7 cycles. However, conventional equation gave un-conservative predictions for the fatigue limit at 10^8 cycles. Therefore, two kinds of modified Murakami's equation were proposed as fatigue limit design curves for the very high cycle fatigue regime. Simple parallel shift of Murakami's equation gave a conservative fatigue limit, whilst better result was obtained by changing the slope of Murakami's equation. The proposed design curve was valid for the defect sizes ranging from 10 to 500 μm .

Keywords: additive manufacturing; Ti-6Al-4V; defect size; fatigue limit design curve; very high cycle fatigue



Citation: Uematsu, Y.; Kakiuchi, T.; Han, Y.; Nakajima, M. Proposal of Fatigue Limit Design Curves for Additively Manufactured Ti-6Al-4V in a VHCF Regime Using Specimens with Artificial Defects. *Metals* **2021**, *11*, 964. <https://doi.org/10.3390/met11060964>

Academic Editors: Ali Mehmanparast and Antonio Mateo

Received: 7 May 2021
Accepted: 11 June 2021
Published: 15 June 2021

Publisher's Note: MDPI stays neutral with regard to jurisdictional claims in published maps and institutional affiliations.



Copyright: © 2021 by the authors. Licensee MDPI, Basel, Switzerland. This article is an open access article distributed under the terms and conditions of the Creative Commons Attribution (CC BY) license (<https://creativecommons.org/licenses/by/4.0/>).

1. Introduction

Additive manufacturing (AM) has been attracting large attention due to its many advantages. Near-net-shape and complicated-shape components can be fabricated by AM using hard-to-work materials, such as high-strength steels, titanium (Ti) alloys and so on [1,2]. It is believed that AM is suitable for large-item and small-scale production, and for trial production especially in the aerospace industries. Ti-6Al-4V is widely used as aerospace components and one of the hard-to-work materials. Therefore, the fabrication of Ti-6Al-4V components by AM is a practical issue, and many prototype components have been manufactured [3]. One of the major drawbacks of AM is the formation of pore-like defects during AM process, which have a significant effect on the fatigue performances [4–7]. That is because pore-like defects could be assumed as fatigue crack starters. It has been reported that hot isostatic pressing (HIP) could reduce the size and number of pores [8,9]. However, the processing cost of AM is relatively high itself, and HIP after AM would further increase the cost. Therefore, as-built components with defects are sometimes used from the viewpoint of reducing costs, indicating the importance of quantitative evaluation of the effect of defects on fatigue properties.

There have been several research studies about the fatigue behaviour of additively manufactured (AMed) Ti-6Al-4V [10–15]. For example, Li et al. [11] surveyed some fatigue test results of wrought and AMed Ti-6Al-4V from the literature and revealed that the

fatigue performances of AMed Ti-6Al-4V were inferior to those of wrought Ti-6Al-4V in the as-built conditions, mainly due to the defect-dominated fatigue crack initiation.

For the fatigue endurance limit design, the definition of fatigue limits of AMed materials with defects is quite important. Murakami and Endo [16,17] proposed an empirical equation using Vickers hardness and the inclusion size as follows to predict fatigue limits at 10^7 cycles of many kinds of steels, in which square root of the area of the inclusion, \sqrt{area} , was assumed as initial fatigue crack length. In the following equations, σ represents the stress amplitude in fatigue tests:

$$\sigma_w(10^7) = \frac{1.43(120 + HV)}{(\sqrt{area})^{1/6}} \quad (1)$$

where $\sigma_w(10^7)$ is the fatigue limit at 10^7 cycles and HV is Vickers hardness.

The above \sqrt{area} model, namely Murakami's equation, is an empirical equation. The defects are assumed as cracks, and the model simulates the transition from the linear elastic fracture mechanics (LEFM) dominating area to fatigue-limit dominating area in Kitagawa–Takahashi diagram [18]. The \sqrt{area} model was proved using specimens with drilled artificial defects or pre-cracks [19], and the proposed model has been widely and practically used for the prediction of fatigue limits of steels. There have been some attempts to apply Murakami's equation for evaluating fatigue limits of non-ferrous alloys with different elastic moduli, such as cast aluminium (Al) alloys having casting defects [20–22] because that equation was empirical. In that research, it was found that some modification should be given to the equation to be used for the precise prediction for Al alloys. Matsunaga et al. [23] conducted uniaxial fatigue tests using Ti-6Al-4V specimens with drilled artificial defects and applied Murakami's equation as the fatigue limit design curve at 10^7 cycles. They concluded that the equation could be used for the prediction without any modification, unlike the case of Al alloys. However, they did not prove the applicability of the equation for the prediction of fatigue limit in the very high cycle fatigue (VHCF) regime, where the number of cycles of fatigue loading was up to 10^8 cycles. Furthermore, the validity was checked only for five different artificial defect sizes and for uniaxial fatigue tests. Accordingly, the transition size of the defect from LEFM dominating area to Murakami's equation was only roughly estimated as 450 μm . Thus, it seems that the confirmation of the applicability of Murakami's equation for Ti-6Al-4V alloy for VHCF regime and for AMed material is insufficient.

In our previous study [24], cantilever-type rotating bending fatigue tests were conducted using AMed Ti-6Al-4V at room temperature and elevated temperature of 523 K (250 °C) under the as-built condition. The maximum defect size in the AMed specimen was estimated by the statistics of extremes [25,26], and it was proved that Murakami's equation was valid to predict the fatigue limits of AMed Ti-6Al-4V at both temperatures. However, it was proved only for one statistically estimated maximum defect size of 85.1 μm , which was defined using 20 samples. To prove that the equation is valid for the wide range of defect sizes, many AMed materials with different statistically estimated maximum defect sizes should be investigated, whilst controlling the maximum defect sizes in the actual AMed materials is difficult. Therefore, in the present study, conventionally manufactured (CMed) Ti-6Al-4V was used.

The drilled artificial hole defects with many different sizes were introduced to the specimens to simulate the wide range of maximum defects in the AMed samples, and cantilever-type rotating bending fatigue tests were conducted using those specimens. In the actual AMed materials, the shapes and types of defects are not limited to pore-like defects, while all defects act as fatigue crack starters irrespective of their shapes and types. The number of cycles to fatigue crack initiation from the defect is dependent on the shapes and types of defects, but the number of cycles to crack initiation is much smaller than the number of cycles to failure, especially in VHCF regime. Therefore, it is reasonable to assume that the drilled artificial defects could simulate many kinds of defects acting as

crack starters. After the fatigue tests, the relationship between fatigue limit and defect size was analysed to propose fatigue limit design curves for the AMed samples having different maximum defect sizes, considering a transition from LFM dominating area to fatigue-limit dominating area. Furthermore, VHCF properties of AMed materials should be investigated for the actual applications [27,28]. Therefore, the applicability of Murakami's equation in the VHCF regime was also investigated.

2. Experimental Procedure

2.1. Material and Specimen

The material used is Ti-6Al-4V alloy, which was conventionally manufactured by forging. The chemical composition is Al: 6.35, V: 4.28, N: 0.009, C: 0.008, H: 0.007, Fe: 0.05, O: 0.16, Ti: Bal. (wt%). The as-received round bar was annealed at 1013 K (740 °C) and would be denoted as CM-Ti in the following text and figures. The reference material is electron beam-melted (EBMed) Ti-6Al-4V, used in the previous study [24], denoted as AM-Ti. The mechanical properties are summarized in Table 1. It should be noted that the properties, especially Vickers hardness, of both materials are nearly comparable. The microstructures of those materials are summarized elsewhere [24]. It is considered that the residual stress of AM-Ti is small because the fabrication process is electron beam melting, in which the energy input is larger than selective laser melting. Furthermore, the residual tensile stress on the as-built sample approaches zero at a depth of 200–500 µm from the surface in the EBMed Ti-6Al-4V [29]. In the present case, surface was removed by the machining followed by careful polishing and buff finishing using alumina suspension [24]. Therefore, the effect of residual stress in the EBMed samples could be negligible.

Table 1. Mechanical properties of materials.

Material	0.2% Proof Stress $\sigma_{0.2}$ [MPa]	Tensile Strength σ_B [MPa]	Elongation δ [%]	Reduction of Area φ [%]	Vickers Hardness HV
AM-Ti	930	970	16	50	351
CM-Ti	917	989	19	52	347

The fatigue specimens are sampled from the annealed round bar, whose configuration is shown in Figure 1. As shown in the figure, one specimen has four drilled artificial defects of different sizes. The specimens could be classified into three types depending on the defect sizes, namely specimens I, II and III having large, medium and small defects, respectively. The designed diameter, depth and corresponding $\sqrt{\text{area}}$ of the defects in each specimen are summarized in Table 2. Figure 2 is a typical result showing the actual shape of a hole defect measured by a laser scanning microscope (LSM: Keyence VK9710, Osaka, Japan). The actual sizes of all the defects, $\sqrt{\text{area}}$, were precisely measured by an LSM; therefore, the measurement error in hole size was quite small. The positions of the holes in the sample were also controlled precisely to minimize the error. The actual hole-like defects in the AMed materials have complicated geometries. However, since the localized stress induced by the complicated geometry is very high, the round shape crack appears immediately at the defects in the very early stage of fatigue life. Similarly, in bending, the complicated geometry of the actual defects at the specimen surface changes its shape to semi-circular immediately under bending fatigue loading. Therefore, drilled artificial defects could simulate the actual defects with complicated shapes [19].

The effect of residual stress in the thin layer around the artificial hole, where fatigue crack initiates, was minimized by removing the hole-edge work-hardened layer on the surface, as per finishing with Emery paper and alumina suspension. Furthermore, it could be considered that the effect of residual stress at the thin layer around the hole was small because crack propagation (not crack initiation), especially non-propagating crack, was taken into account in the $\sqrt{\text{area}}$ model, as will be shown in Section 3.2 using Figures 6 and 7.

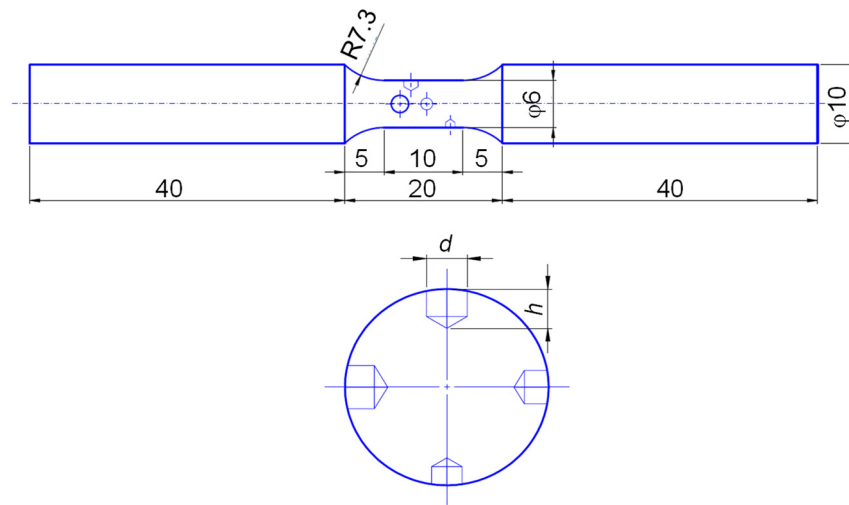


Figure 1. Fatigue specimen configuration with drilled artificial defects. Dimension is in mm.

Table 2. Sizes of artificial defects of specimens I, II and III.

Specimen I Large			Specimen II Medium			Specimen III Small		
<i>d</i> (mm)	<i>h</i> (mm)	\sqrt{area} (mm)	<i>d</i> (mm)	<i>h</i> (mm)	\sqrt{area} (mm)	<i>d</i> (mm)	<i>h</i> (mm)	\sqrt{area} (mm)
2.2	2.1	2.1	1.2	1.1	1.1	0.3	0.3	0.3
1.8	1.7	1.7	0.9	0.8	0.8	0.2	0.2	0.2
1.5	1.4	1.4	0.6	0.6	0.6	0.1	0.1	0.1
1.2	1.1	1.1	0.4	0.4	0.4	0.08	0.05	0.06

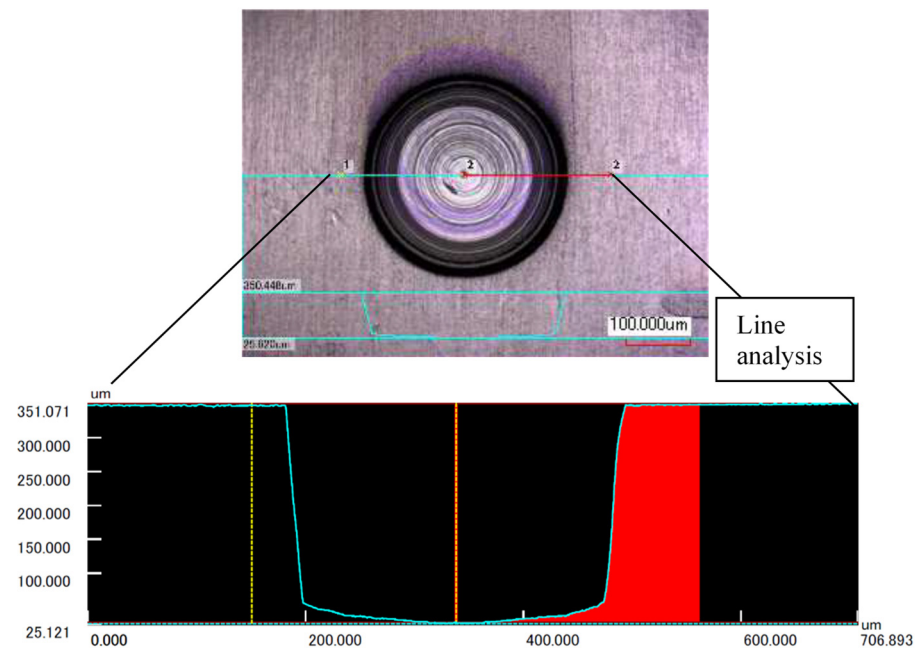


Figure 2. An example of the shape of a hole defect measured by an LSM.

2.2. Test Procedures

Cantilever-type rotating bending fatigue tests were conducted at a frequency, $f = 52.5$ Hz (3150 rpm) using a fatigue testing machine called the GIGA QUAD YRB200

(Yamamoto Metal Technos Co., Ltd., Osaka, Japan). As shown in Figure 3 [21], the larger defect experiences a lower bending moment in the cantilever-type rotating bending fatigue tests, with the hope that all the defects could be potential fatigue crack initiation sites. After fatigue tests, the defects in the fatigue-failed and run-out samples were examined in detail by a scanning electron microscope (SEM: JEOL JSM-6060, Tokyo, Japan), whether fatigue crack initiated at the defect or not. The run-out cycle was defined as 10^8 , while the fatigue crack initiation was checked by an SEM at both 10^7 and 10^8 cycles.

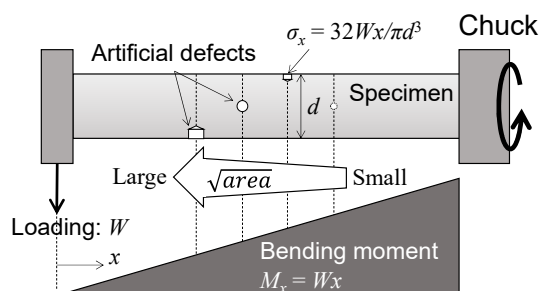


Figure 3. Schematic illustration of moment distribution at each artificial defect.

3. Results

3.1. Crack Initiation at Artificial Defects

Figure 4 shows the simple relationships between stress amplitudes and the number of cycles to failure in the samples with artificial defects, in which the stress amplitude represents the nominal stress at the centre of each defect with different bending moments (see Figure 3). Therefore, one sample has four data plots. Red cross symbols in the figure are the defects, where the main crack was initiated and propagated until final failure. The specimens having smaller defects exhibit higher fatigue strengths. This figure is not for drawing regular $S-N$ diagram, but is shown only for summarizing experimental data sets, which are used to draw the Kitagawa–Takahashi diagram. The details will be mentioned in Section 4.

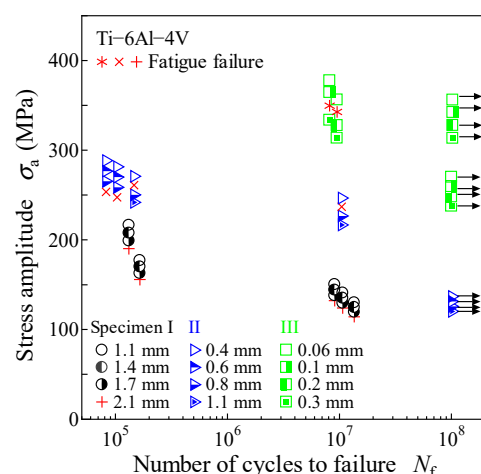


Figure 4. Experimental data sets used to draw Kitagawa–Takahashi diagram.

The typical fatigue fracture surface is shown in Figure 5, whose fatigue crack initiated at the defect with the size of $\sqrt{area} \approx 0.6$ mm. Subsequently, all the defects of the fatigue-failed and run-out samples were examined in detail. Figure 6 indicates a defect having fatigue cracks at 8.0×10^4 cycles, and Figure 7a–c are those at 1.0×10^5 , 1.5×10^5 and 9.0×10^6 cycles, respectively. In those cases, the main fatigue cracks initiated at the other defects and propagated until final failure. The lengths of those secondary cracks in Figures 6 and 7 are ranging from 10 to a few hundred microns. The cracks were not

found in the run-out samples. However, the fatigue crack with a length of $20\ \mu\text{m}$ was found at 9.0×10^6 cycles Figure 7c, and it might be equivalent to non-propagating crack at 10^7 cycles.

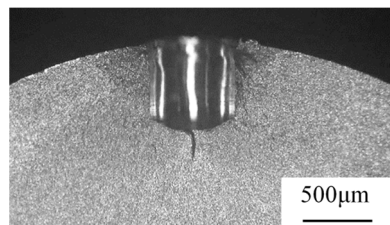


Figure 5. Typical fatigue crack initiation from an artificial defect ($\sqrt{\text{area}} \approx 0.6\ \text{mm}$).

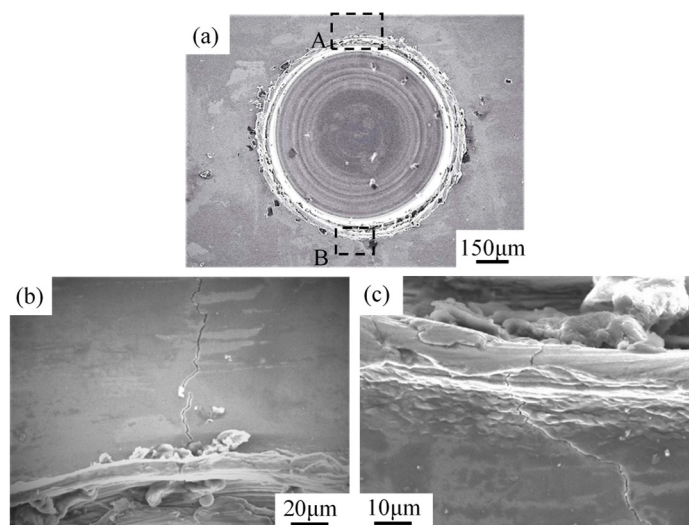


Figure 6. Secondary fatigue cracks found at an artificial defect ($d = 0.73\ \text{mm}$, $N = 8.0 \times 10^4$, specimen Type II in Table 2). (a) Macroscopic view; (b) magnified view of area A in Figure (a); (c) magnified view of area B in Figure (a).

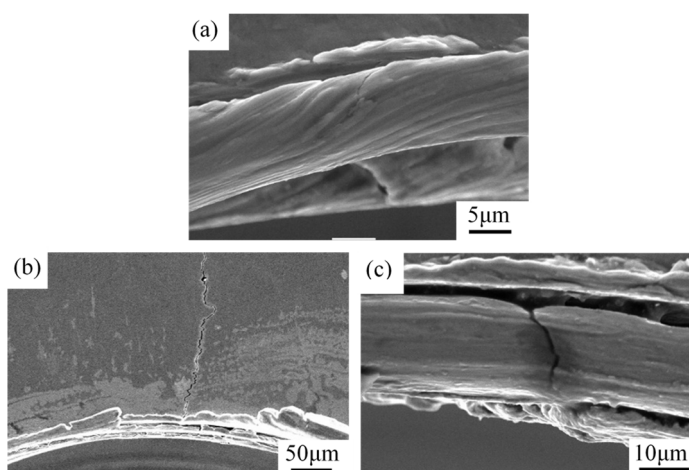


Figure 7. Some examples of secondary fatigue cracks found at artificial defects; (a) $d = 0.48\ \text{mm}$, $N = 1.0 \times 10^5$, (b) $d = 1.28\ \text{mm}$, $N = 1.5 \times 10^5$, (c) $d = 1.26\ \text{mm}$, $N = 9.0 \times 10^6$ ((a–c) are all specimen type ii in Table 2).

3.2. Stress Amplitude as a Function of $\sqrt{\text{area}}$

Figure 8a shows the relationship between stress amplitude and $\sqrt{\text{area}}$ of defect at 10^7 cycles. Four data points correspond to one specimen with four defects of different sizes.

Cross symbols in the figure represent the defects at which the main fatigue crack initiated and propagated until final failure. Circular hollow symbols are the defects that survived 10^7 cycles without any fatigue crack initiation. Red triangular symbols mean that fatigue cracks initiated at those defects, but the main crack leading to the final failure initiated at the other defects. Small blue solid dots mean that fatigue crack did not initiate at those defects, but fatigue failure occurred before 10^7 cycles at the other defects with the main crack. Figure 8b is the same figure at 10^8 cycles. It should be noted that some specimens survived 10^7 cycles in Figure 8a, whilst failed before 10^8 cycles in Figure 8b, namely fatigue failure, took place in the VHCF regime. The following discussion will be made based on Figure 8a,b.

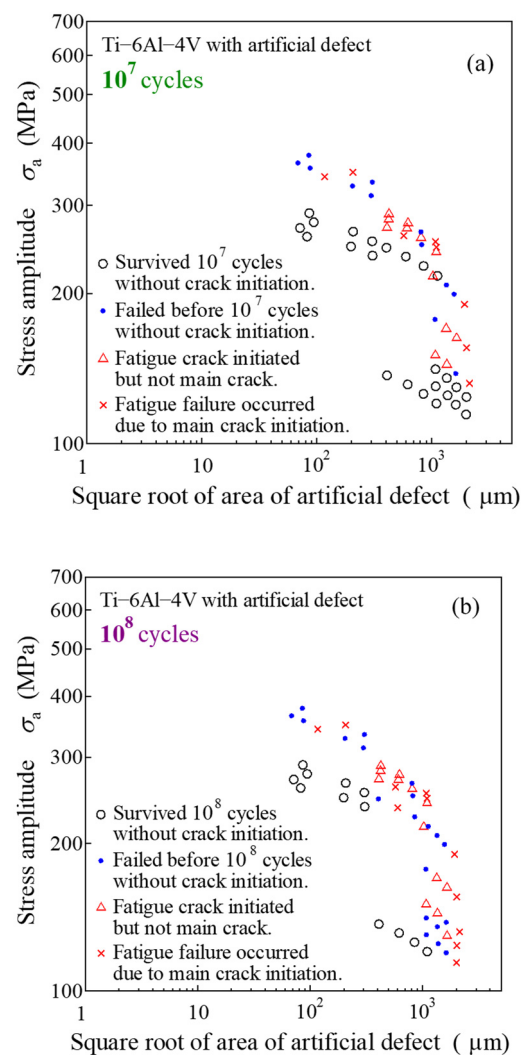


Figure 8. Relationship between stress amplitude and $\sqrt{\text{area}}$ of the defect; (a) 10^7 cycles, (b) 10^8 cycles.

4. Discussion

4.1. Kitagawa–Takahashi–Murakami Diagram at 10^7 Cycles

Figure 9 is the S - N diagram of CM-Ti and EBMed Ti-6Al-4V, namely AM-Ti, at room temperature in the previous study [24]. The fatigue limits of CM-Ti were 625 MPa and 575 MPa, and those of AM-Ti were 300 MPa and 225 MPa at 10^7 and 10^8 cycles, respectively. The number of data points is limited, but the approximate curve of discrete data points in Figure 9 is defined as 50% fracture probability curve in the P - S - N curves. Therefore, the above fatigue limits are the approximations of the precise fatigue limits obtained by a staircase method. The defect sizes at the crack initiation sites of AM-Ti in Figure 9 were

measured as typically shown in Figure 10, in which the defect size, \sqrt{area} , as defined by the envelope of the defect. The effective defect size at the crack initiation site was proposed by Masuo et al. [30]. Still, it was not considered in the present case because the statistical analyses of the defect sizes were done using the envelope shown in Figure 10 [24]. Figure 11 summarises the results of CM-Ti with artificial defects and AM-Ti at 10^7 cycles, as a relationship between stress amplitude and defect size. In this figure, the Kitagawa–Takahashi diagram is drawn in Figure 8a. The threshold value of long fatigue crack propagation (FCP), $K_{max, th} = 6.2 \text{ MPam}^{1/2}$ was obtained by the FCP tests of Ti-6Al-4V with a similar microstructure using compact tension (CT) specimens at the load ratio, $R = 0.05$ [31,32]. It should be noted that FCP at the stress ratio, $R = -1$, could be estimated using the results at $R = 0.05$ because the stress intensity factor in the negative portion could be neglected because of crack closure.

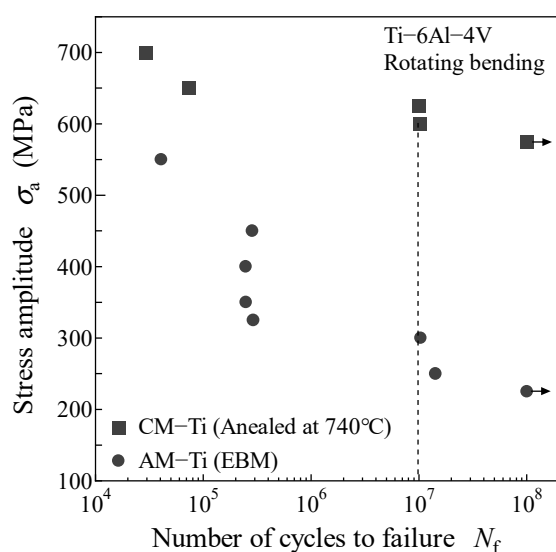


Figure 9. S-N diagram of conventionally manufactured and EBMed Ti-6Al-4V.

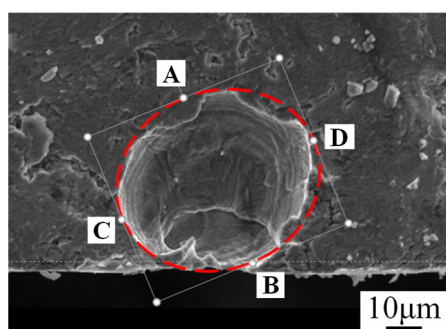


Figure 10. Defect at fatigue crack initiation site of EBMed Ti-6Al-4V ($\sigma_a = 450 \text{ MPa}$, $N_f = 2.8 \times 10^5$).

The following equation was used for the stress intensity factor calculation in Figure 11, assuming the surface defects [19].

$$K_{max} = 0.65\sigma\sqrt{\pi\sqrt{area}} \quad (2)$$

Two solid symbols of AM-Ti at the stress amplitudes of 250 and 300 MPa (green circular symbols) mean that fatigue failure did not occur at 10^7 cycles. However, the fatigue tests were continued beyond 10^7 cycles until final fatigue failure, as will be discussed in the next section. Therefore, the actual defect sizes at the crack initiation sites are plotted for those data after fatigue failure in VHCF regime. Murakami's Equation (1) is given in the

figure as a red dotted line, in which the Vickers hardness of AM-Ti, $HV351$ (Table 1) is used. It should be noted that AM-Ti and CM-Ti have comparable hardness, as shown in Table 1, which enables direct comparison between AM-Ti and CM-Ti using Murakami's equation.

In the present study, the statistically estimated maximum defect size of AM-Ti is $85.1 \mu\text{m}$ and the predicted fatigue limit (10^7), based on Murakami's equation, is shown by a black solid square symbol at 321 MPa [24]. It is clear that fatigue failure of AM-Ti (green cross symbols) and fatigue failure or fatigue crack initiation of CM-Ti with artificial defects (red cross and triangular symbols) occurred in the upper areas of Murakami's equation and LEFM line of Kitagawa–Takahashi diagram. The results correspond with those by Matsunaga et al. [23]. In the present study, the transition defect size from LEFM-dominating area to Murakami's equation could be clearly defined as $523 \mu\text{m}$, whilst the rough estimation by Matsunaga et al. [23] was about $450 \mu\text{m}$. Figure 11 implies that conventional Murakami's equation could be used as a fatigue limit (10^7) design curve for AMed Ti-6Al-4V with different defect sizes. Masuo et al. also showed that the fatigue failure of EBMed Ti-6Al-4V occurred when the stress amplitudes were higher than the predicted fatigue limit (10^7) by Equation (1) [32].

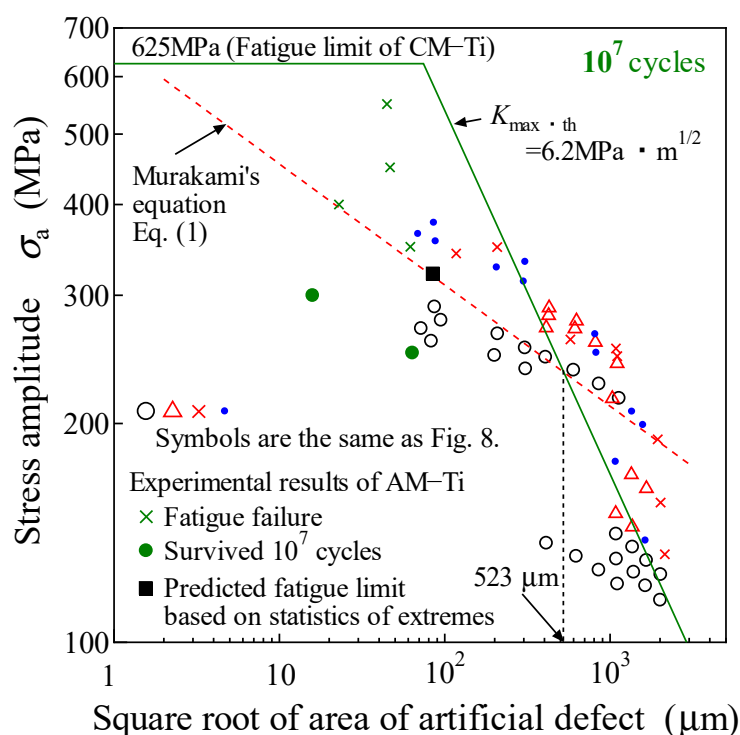


Figure 11. Kitagawa–Takahashi–Murakami diagram at 10^7 cycles.

4.2. Kitagawa–Takahashi–Murakami Diagram at 10^8 Cycles

As mentioned above, fatigue tests of CM-Ti with artificial defects and AM-Ti were continued up to 10^8 cycles to investigate the applicability of Murakami's equation in VHCF regime. Figure 12 shows Kitagawa–Takahashi–Murakami diagram at 10^8 cycles. In Figure 11, the fatigue tests of AM-Ti at the stress amplitudes of 250 MPa and 300 MPa survived 10^7 cycles, but failed before 10^8 cycles, as shown by green bold cross symbols in Figure 12. As the fatigue specimen tested at 225 MPa survived 10^8 cycles, the actual defect size at the crack initiation site was unknown. Therefore, the data was plotted as a green solid circular symbol in the figure assuming the defect size of $85.1 \mu\text{m}$, which was estimated based on the statistics of extremes [24].

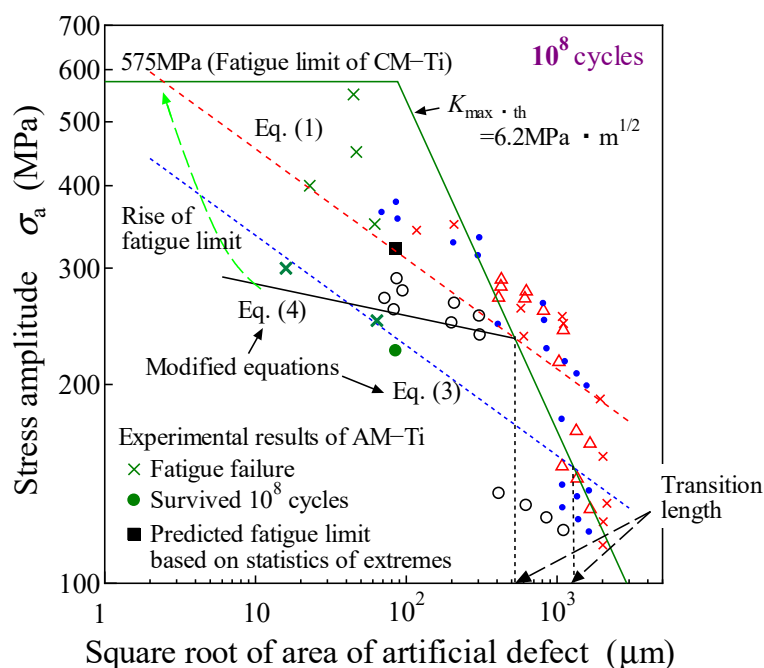


Figure 12. Kitagawa–Takahashi–Murakami diagram at 10^8 cycles.

Some results of CM-Ti with artificial defects in Figure 11 changed from run-out to failure or to fatigue crack initiation, as shown in Figure 12. In addition, the fatigue failure of AM-Ti occurred below Murakami’s equation in VHCF regime, indicating that the prediction of fatigue limits at 10^8 cycles using that conventional equation would not be sufficient. Thus, the following modified Murakami’s equation is proposed as a fatigue limit (10^8) design curve at 10^8 cycles, which is shown as a blue dotted line in Figure 12.

$$\sigma_w(10^8) = \frac{1.43(-5.6 + HV)}{(\sqrt{area})^{1/6}} \tag{3}$$

This equation is a simple parallel shift of Murakami’s equation obtained by the fitting of some data points (two bold green cross symbols, one green solid circular symbol and two triangular red symbols below the dashed blue line in Figure 12) and keeping the slope of Murakami’s equation. Since some circular hollow symbols (un-failed data of CM-Ti with artificial defects at 10^8 cycles) are in the upper area of the proposed equation, Equation (3) can give conservative fatigue limits (10^8), which implies the practical merit of this equation. However, a simple parallel shift means that the transition crack length from the LFM-dominating area to Murakami’s equation becomes longer with increasing loading cycles as shown by the dashed black arrows in Figure 12. The transition crack length seems to be constant from the viewpoint of the basic concept of LFM. Thus, the following equation is shown in the figure as a solid black line, which is crossing the transition crack length of 523 μm at 10^7 cycles, and is drawn to roughly divide the areas of fatigue failure and un-failure.

$$\sigma_w(10^8) = \frac{1.43(-129 + HV)}{(\sqrt{area})^{1/21}} \tag{4}$$

Although some plots indicating the non-failure of CM-Ti with artificial defects are seen in the upper area of the proposed line by Equation (4), the equation still gives a conservative and better estimation of fatigue limits at 10^8 cycles than Equation (3). It should be noted that this design curve is valid only for the defect sizes ranging from 10 to 500 μm . For the smaller defects than 10 μm , Equation (4)’s prediction of fatigue limits (10^8) are too conservative, which are much lower than the fatigue limit of the smooth specimen (575 MPa). We anticipated that a drastic rise in the fatigue limit (10^8) would take place

when the defect size became smaller than 10 μm , as shown by the dashed green curve in the figure. However, Equation (4) could be used for the practical cases because typical defect sizes in the AMed materials are approximately a few tens of microns [10–15].

Consequently, the fatigue limit (10^8) prediction procedure is as follows. First, the maximum defect size in the AMed fatigue specimen should be estimated using statistics of extremes [19], and subsequently, the fatigue limit (10^8) of VHCF regime could be predicted by Equation (4). This fatigue limit (10^7) prediction procedure is similar to that of steels having inclusions (usually intermetallic compounds), in which inclusions are assumed to be non-propagating cracks. In the present case, defects in the AMed samples and artificial defects in CMed samples could be assumed to be non-propagating cracks as well.

5. Conclusions

Cantilever-type rotating bending fatigue tests were conducted using conventionally manufactured (CMed) Ti-6Al-4V. Four drilled artificial defects with different sizes were introduced to each specimen. The defects were classified into three types after fatigue tests. First, the defect at which the main crack initiated and grew to the final failure. Second, the defect at which fatigue crack initiated but not related to the final failure (secondary crack initiation). Third, the defects survived up to 10^7 or 10^8 cycles without fatigue crack initiation. Finally, the results were used to draw fatigue limit design curves of additively manufactured (AMed) Ti-6Al-4V in a very high cycle fatigue regime considering the transition from LEFM-dominating area to fatigue-limit dominating area. The conclusions are as follows.

- (1) Fatigue limits of AMed Ti-6Al-4V at 10^7 and 10^8 cycles were lower than those of CMed Ti-6Al-4V, because the defects acted as fatigue crack starters.
- (2) Kitagawa–Takahashi diagram was drawn, and the fatigue test results of CMed Ti-6Al-4V with artificial defects were compared with those of AMed Ti-6Al-4V. The transition from the LEFM-dominating area to the fatigue limit dominating area was well described by the conventional Murakami's equation at 10^7 cycles. However, conventional equation gave an insufficient prediction of the fatigue limit at 10^8 cycles.
- (3) Two kinds of modified Murakami's equations were proposed as fatigue limit design curves at 10^8 cycles. A parallel shift of Murakami's equation was simple and gave conservative results. However, a parallel shift means that the transition crack length from LEFM-dominating area to Murakami's equation becomes longer with increasing loading cycles. A better prediction could be given by changing the slope of Murakami's equation in keeping with the transition crack length constant, and the modified equation was valid for the defect sizes ranging from 10 to 500 μm .

Author Contributions: Fatigue test planning, Y.U., T.K. and M.N.; conducting fatigue tests, Y.H.; analysis, Y.U.; writing, Y.U.; review and editing, T.K and M.N. All authors have read and agreed to the published version of the manuscript.

Funding: This research received no external funding.

Institutional Review Board Statement: Not applicable.

Informed Consent Statement: Not applicable.

Data Availability Statement: Data sharing is not applicable to this article.

Acknowledgments: The authors wish to thank Akira UENO (Ritsumeikan University), who suddenly passed away in July 2020, for kind advice on the experimental method using specimens with artificial defects, and analyses using Murakami's concept.

Conflicts of Interest: The authors declare no conflict of interest.

References

1. Murr, L.E.; Gaytan, S.M.; Ramirez, D.A.; Martinez, E.; Hernandez, J.; Amato, K.N.; Shindo, P.W.; Medina, F.R.; Wicker, R.B. Metal Fabrication by Additive Manufacturing Using Laser and Electron Beam Melting Technologies. *J. Mater. Sci. Technol.* **2012**, *28*, 1–14. [[CrossRef](#)]
2. Herzog, D.; Seyda, V.; Wycisk, E.; Emmelmann, C. Additive manufacturing of metals. *Acta Mater.* **2016**, *117*, 371–392. [[CrossRef](#)]
3. Liu, S.; Shin, Y.C. Additive manufacturing of Ti6Al4V alloy: A review. *Mater. Des.* **2019**, *164*, 107552. [[CrossRef](#)]
4. Akita, M.; Uematsu, Y.; Kakiuchi, T.; Nakajima, M.; Kawaguchi, R. Defect-dominated fatigue behavior in type 630 stainless steel fabricated by selective laser melting. *Mater. Sci. Eng. A* **2016**, *666*, 19–26. [[CrossRef](#)]
5. Croccolo, D.; De Agostinis, M.; Fini, S.; Olmi, G.; Vranic, A.; Ciric-Kostic, S. Influence of the build orientation on the fatigue strength of EOS maraging steel produced by additive metal machine. *Fatigue Fract. Eng. Mater. Struct.* **2016**, *39*, 637–647. [[CrossRef](#)]
6. Tang, M.; Pistorius, P.C. Oxides, porosity and fatigue performance of AlSi10Mg parts produced by selective laser melting. *Int. J. Fatigue* **2017**, *94*, 192–201. [[CrossRef](#)]
7. Zhang, M.; Sun, C.-N.; Zhang, X.; Wei, J.; Hardacre, D.; Li, H. Predictive models for fatigue property of laser powder bed fusion stainless steel 316L. *Mater. Des.* **2018**, *145*, 42–54. [[CrossRef](#)]
8. Fatemi, A.; Molaei, R.; Simsirivong, J.; Sanaei, N.; Pegues, J.; Torries, B.; Phan, N.; Shamsaei, N. Fatigue behaviour of additive manufactured materials: An overview of some recent experimental studies on Ti-6Al-4V considering various processing and loading direction effects. *Fatigue Fract. Eng. Mater. Struct.* **2019**, *42*, 991–1009. [[CrossRef](#)]
9. Benzing, J.; Hrabec, N.; Quinn, T.; White, R.; Rentz, R.; Ahlfors, M. Hot isostatic pressing (HIP) to achieve isotropic micro-structure and retain as-built strength in an additive manufacturing titanium alloy (Ti-6Al-4V). *Mater. Lett.* **2019**, *257*, 126690. [[CrossRef](#)]
10. Leuders, S.; Thöne, M.; Riemer, A.; Niendorf, T.; Tröster, T.; Richard, H.A.; Maier, H.J. On the mechanical behaviour of titanium alloy TiAl6V4 manufactured by selective laser melting: Fatigue resistance and crack growth performance. *Int. J. Fatigue* **2013**, *48*, 300–307. [[CrossRef](#)]
11. Li, P.; Warner, D.; Fatemi, A.; Phan, N. Critical assessment of the fatigue performance of additively manufactured Ti-6Al-4V and perspective for future research. *Int. J. Fatigue* **2016**, *85*, 130–143. [[CrossRef](#)]
12. Hrabec, N.; Gnäupel-Herold, T.; Quinn, T. Fatigue properties of a titanium alloy (Ti-6Al-4V) fabricated via electron beam melting (EBM): Effects of internal defects and residual stress. *Int. J. Fatigue* **2017**, *94*, 202–210. [[CrossRef](#)]
13. Biswal, R.; Zhang, X.; Syed, A.K.; Awd, M.; Ding, J.; Walther, F.; Williams, S. Criticality of porosity defects on the fatigue performance of wire + arc additive manufactured titanium alloy. *Int. J. Fatigue* **2019**, *122*, 208–217. [[CrossRef](#)]
14. Dallago, M.; Winiarski, B.; Zanini, F.; Carmignato, S.; Benedetti, M. On the effect of geometrical imperfections and defects on the fatigue strength of cellular lattice structures additively manufactured via Selective Laser Melting. *Int. J. Fatigue* **2019**, *124*, 348–360. [[CrossRef](#)]
15. Li, P.; Warner, D.; Pegues, J.; Roach, M.; Shamsaei, N.; Phan, N. Towards predicting differences in fatigue performance of laser powder bed fused Ti-6Al-4V coupons from the same build. *Int. J. Fatigue* **2019**, *126*, 284–296. [[CrossRef](#)]
16. Murakami, Y.; Endo, M.; Murakami, Y.; Endo, M. Effects of defects, inclusions and inhomogeneities on fatigue strength. *Int. J. Fatigue* **1994**, *16*, 163–182. [[CrossRef](#)]
17. Murakami, Y. Material defects as the basis of fatigue design. *Int. J. Fatigue* **2012**, *41*, 2–10. [[CrossRef](#)]
18. Kitagawa, H.; Takahashi, S. Applicability of fracture mechanics to very small cracks or cracks in the early stage. In Proceedings of the Second International Conference on Mechanical Behavior of Materials, ASM 1976, Boston, MA, USA, 16–20 August 1976; pp. 627–631.
19. Murakami, Y. *Metal Fatigue: Effects of Small Defects and Nonmetallic Inclusions*; Elsevier: Amsterdam, The Netherlands, 2002.
20. Tajiri, A.; Nozaki, T.; Uematsu, Y.; Kakiuchi, T.; Nakajima, M.; Nakamura, Y.; Tanaka, H. Fatigue Limit Prediction of Large Scale Cast Aluminum Alloy A356. *Procedia Mater. Sci.* **2014**, *3*, 924–929. [[CrossRef](#)]
21. Ueno, A.; Nishida, M.; Miyakawa, S.; Yamada, K.; Kikuchi, S. Fatigue Limit Estimation of Aluminum Die-casting Alloy by Means of $\sqrt{\text{area}}$ Method. *J. Soc. Mater. Sci. Jpn.* **2014**, *63*, 844–849. [[CrossRef](#)]
22. Uematsu, Y.; Kakiuchi, T.; Tajiri, A.; Nakajima, M. Fatigue limit prediction of A356-T6 cast aluminum alloys with different defect sizes sampled from an actual large-scale component. *Int. J. Struct. Integr.* **2017**, *8*, 617–631. [[CrossRef](#)]
23. Matsunaga, H.; Murakami, Y.; Kubota, M.; Lee, J.H. Fatigue strength of Ti-6Al-4V alloys containing small artificial defects. *Mat. Sci. Res. Int.* **2003**, *9*, 263–269. [[CrossRef](#)]
24. Kakiuchi, T.; Kawaguchi, R.; Nakajima, M.; Hojo, M.; Fujimoto, K.; Uematsu, Y. Prediction of fatigue limit in additively manufactured Ti-6Al-4V alloy at elevated temperature. *Int. J. Fatigue* **2019**, *126*, 55–61. [[CrossRef](#)]
25. Murakami, Y.; Usuki, H. Quantitative evaluation of effects of non-metallic inclusions on fatigue strength of high strength steels. II: Fatigue limit evaluation based on statistics for extreme values of inclusion size. *Int. J. Fatigue* **1989**, *11*, 299–307. [[CrossRef](#)]
26. Murakami, Y. Inclusion rating by statistics of extreme values and its application to fatigue strength prediction and quality control of materials. *J. Res. Natl. Inst. Stand. Technol.* **1994**, *99*, 345. [[CrossRef](#)]
27. Günther, J.; Krewerth, D.; Lippmann, T.; Leuders, S.; Tröster, T.; Weidner, A.; Biermann, H.; Niendorf, T. Fatigue life of additively manufactured Ti-6Al-4V in the very high cycle fatigue regime. *Int. J. Fatigue* **2017**, *94*, 236–245. [[CrossRef](#)]
28. Nicoletto, G. Anisotropic high cycle fatigue behavior of Ti-6Al-4V obtained by powder bed laser fusion. *Int. J. Fatigue* **2017**, *94*, 255–262. [[CrossRef](#)]

29. Vastola, G.; Zhang, G.; Pei, Q.X.; Zhang, Y.W. Controlling of residual stress in additive manufacturing of Ti6Al4V by finite element modelling. *Addit. Manuf.* **2016**, *12*, 231–239.
30. Masuo, H.; Tanaka, Y.; Morokoshi, S.; Yagura, H.; Uchida, T.; Yamamoto, Y.; Murakami, Y. Influence of defects, surface roughness and HIP on the fatigue strength of Ti-6Al-4V manufactured by additive manufacturing. *Int. J. Fatigue* **2018**, *117*, 163–179. [[CrossRef](#)]
31. Sugeta, A.; Jono, M.; Uematsu, Y.; Yamamoto, M.; Ueda, H. Effect of Microstructure on Fatigue Crack Growth Behavior in Ti-6Al-4V Alloy. *J. Soc. Mater. Sci. Jpn.* **1998**, *47*, 273–278. [[CrossRef](#)]
32. Sugeta, A.; Uematsu, Y.; Kitayama, Y.; Jono, M. Fatigue Crack Growth Behavior of Ti-6Al-4V Alloy with Bimodal Microstructure under Repeated Two-step Load Sequences. *Trans. Jpn. Soc. Mech. Eng. Ser. A* **2005**, *71*, 1153–1159. (In Japanese) [[CrossRef](#)]